PHYSICAL REVIEW A **91**, 012710 (2015)

Electron-ion collision spectroscopy: Lithium-like xenon ions

D. Bernhardt,[1,2] C. Brandau,[1,2,*] Z. Harman,[2,3] C. Kozhuharov,[4] S. Böhm,[1] F. Bosch,[4] S. Fritzsche,[5,6] J. Jacobi,[1] S. Kieslich,[1]
H. Knopp,[1] F. Nolden,[4] W. Shi,[1] Z. Stachura,[7] M. Steck,[4] Th. Stöhlker,[4,5,8] S. Schippers,[1] and A. Müller[1]
[1]*Institut für Atom- und Molekülphysik, Justus-Liebig-University Giessen, Leihgesterner Weg 217, D-35392 Giessen, Germany*
[2]*ExtreMe Matter Institute EMMI and Research Division, GSI Helmholtzzentrum für Schwerionenforschung,*
Planckstraße 1, D-64291 Darmstadt, Germany
[3]*Max-Planck-Institut für Kernphysik, Saupfercheckweg 1, D-69117 Heidelberg, Germany*
[4]*GSI Helmholtzzentrum für Schwerionenforschung, Planckstraße 1, D-64291 Darmstadt, Germany*
[5]*Helmholtz-Institut Jena, Fröbelstieg 3, D-07743 Jena, Germany*
[6]*Physikalisch-Astronomische Fakultät, Friedrich-Schiller-Universität, Fröbelstieg 3, D-07743 Jena, Germany*
[7]*Instytut Fizyki Jądrowej, Radzikowskiego 152, PL-31-342 Kraków, Poland*
[8]*Institut für Optik und Quantenelektronik, Friedrich-Schiller-Universität Jena, Max-Wien-Platz 1, D-07743 Jena, Germany*
(Received 27 November 2014; published 20 January 2015)

The resonant process of dielectronic recombination (DR) has been applied as a spectroscopic tool to investigate intra-L-shell excitations $2s$-$2p_j$ in Li-like $^{136}\mathrm{Xe}^{51+}$. The experiments were carried out at the electron cooler of the Experimental Storage Ring of the GSI-Helmholtzzentrum für Schwerionenforschung, Darmstadt, Germany. The observed center-of-mass energy range (0–505 eV) covers all resonances associated with the $2s + e^- \rightarrow (2p_{1/2}nl_j)_J$ and $(2p_{3/2}nl_j)_J$ DR processes. Energies and strengths of isolated $2p_{1/2}n$ and $2p_{3/2}n$ DR-resonance groups were obtained for principal quantum numbers n up to 43 and 36, respectively. The $2s$-$2p_{1/2}$ and $2s$-$2p_{3/2}$ excitation energies were deduced to be 119.816(42) eV and 492.174(52) eV. The excitation energies are compared with previous measurements of other groups and with recent QED calculations. In addition, the experimental spectra and extracted resonance strengths are compared with multiconfiguration Dirac-Fock calculations. Measurements and theory are found to be in good agreement with each other.

DOI: 10.1103/PhysRevA.91.012710 PACS number(s): 34.80.Lx, 31.10.+z, 31.30.J–

I. INTRODUCTION

In atoms, relativistic corrections to the nonrelativistic Coulomb binding energies, the dominant self-energy corrections, and vacuum polarization contributions of quantum electrodynamics (QED) scale predominantly with the fourth power of the nuclear charge number Z [1,2]. At the same time, the electric field strength, which is the reference parameter of a field theory, increases for s electrons by nearly 7 orders of magnitude from hydrogen to uranium. The interaction strength αZ between electrons and the nucleus transits from the the perturbative regime to the nonperturbative domain. These facts motivate the study of relativistic and QED effects in heavy atoms and, in particular, in few-electron heavy ions. Here we report on experimental measurements of the $2s \rightarrow 2p_{1/2}$ and $2s \rightarrow 2p_{3/2}$ excitation energies in Li-like Xe^{51+} ions employing electron-ion collision spectroscopy at a heavy-ion storage ring. With this medium-Z ion we intend to bridge the gap between similar work on low-Z [3] and high-Z [4] Li-like ions.

Since the seminal work of Schweppe *et al.* [5], who benchmarked the $2s$-$2p_{1/2}$ splitting in U^{89+}, Li-like systems have attracted much attention from the experimental as well as from the theoretical side. To date, the most precise values for the $2s \rightarrow 2p_{1/2}$ and $2s \rightarrow 2p_{3/2}$ splittings in heavy Li-like ions have been obtained, for example, by use of x-ray spectroscopy at an electron-beam ion trap (EBIT) [6,7] either by direct observation of the emitted photons or by application of x-ray laser spectroscopy at a free electron laser [8], by beam foil spectroscopy [5,9–11], and by electron-ion collision spectroscopy in heavy-ion storage rings [3,4]. The experimental results are sensitive to second-order QED effects [12–14].

Our approach, electron-ion collision spectroscopy, exploits the spectroscopic properties of dielectronic recombination (DR). DR is a resonant electron-ion collision process. DR collision spectroscopy at heavy-ion storage rings is a well-established spectroscopic tool [3,4,15–17]. It is a versatile alternative to approaches that measure the wavelength of emitted or absorbed photons. The list of questions tackled with DR comprises such diverse topics as strong-field quantum electrodynamics, relativistic atomic physics, the influence of external fields on the recombination process, nuclear physics, and astrophysics [3,4,15,17–21]. For further details and more references please refer to the reviews in Refs. [16,22–24].

DR proceeds in two steps,

$$e^- + A^{q+} \rightarrow [A^{(q-1)+}]^{**} \rightarrow [A^{(q-1)+}]^{*} + \text{photon(s)},$$

where in the first step the initially free electron is captured into a bound state of the ion with simultaneous excitation of a core electron. This initial resonant dielectronic capture (DC) forms the foundation of DR as a spectroscopic tool. DC is time inverse to autoionization, and, thus, DR studies as conducted at storage rings can be regarded as Auger spectroscopy in inverse kinematics. In the second step the recombined doubly-excited ion is stabilized by radiative deexcitation. The resonance energy for DR, E_{DR}, depends on the energy needed for the excitation of the initially bound electron E_{ex} and the binding energy of the captured initially free electron E_B:

$$E_{\mathrm{DR}} = E_{\mathrm{ex}} - E_B. \quad (1)$$

---

[*] c.brandau@gsi.de

DR spectroscopy determines E_{ex} by using precise measurements of E_{DR} and calculated Rydberg binding energies E_B, which are less affected by QED and correlation effects and therefore can be calculated to low uncertainties [3]. Alternatively, the Rydberg energies can be extrapolated to the series limit $n \to \infty$ where $E_B = 0$, thus yielding E_{ex} [4]. In the present measurement DR of Li-like $^{136}\text{Xe}^{51+}$ forming $^{136}\text{Xe}^{50+}$ by the following processes:

$$\text{Xe}^{51+}(1s^2\,2s) + e^- \to \text{Xe}^{50+}\left(1s^2\,2p_{\bar{j}}\,nl_j\right)_J^{**} \\ \to \text{Xe}^{50+*} + \text{photons}$$

is studied. The angular momentum of the L-shell electron is labeled $\bar{j}$ with $\bar{j} = 1/2,3/2$, and the angular momentum of the Rydberg-electron is given by j. J denotes the total angular momentum of the doubly excited intermediate state. The investigated energy range of 0–505 eV of our experiment covers all DR resonances associated with the two $\Delta n = 0$ DR Rydberg resonance series $(2p_{1/2}nl_j)_J$ and $(2p_{3/2}nl_j)_J$.

In our data analysis we benefit from this measurement of the full series of Rydberg resonances inasmuch as we utilize the regular pattern for an improved calibration of our energy axis (Sec. IV C). From the measured DR resonances we extract the $2s \to 2p_{1/2}$ and $2s \to 2p_{3/2}$ excitation energies (see Sec. IV D).

The absolute measurement of the Xe^{51+} recombination rate coefficient with high resolution allowed us to determine strengths and energies for numerous individual resonance groups of the $2p_{1/2}n$ and $2p_{3/2}n$ resonance series. The experimental results are compared with state-of-the-art multiconfiguration Dirac-Fock (MCDF) calculations.

II. CALCULATION OF DIELECTRONIC RECOMBINATION CROSS SECTIONS

For the calculation of DR cross sections we employ the independent-processes isolated-resonances approximation which neglects interference between DR and nonresonant radiative recombination (RR) as well as interference between overlapping DR resonances of the same symmetry.

A given DR channel proceeds from the Li-like initial level ($1s^22s$, i) through the doubly-excited intermediate level of type $1s^22p_{\bar{j}}nl_j$ (indexed by d) to a final level (f) formed after radiative decay. The cross section for such a channel is given as a function of the electron kinetic energy $E_{\text{c.m.}}$ in the ion rest frame as (in atomic units; see, e.g., Refs. [25,26])

$$\sigma_{\text{DR}}^{i\to d\to f}(E_{\text{c.m.}}) = S_{\text{DR}}^{i\to d\to f}\,L_d(E_{\text{c.m.}})\,, \tag{2}$$

with the resonance strength, i.e., the integrated cross section for a selected peak, given as

$$S_{\text{DR}}^{i\to d\to f} = \frac{2\pi^2}{p^2}\,\frac{2J_d+1}{2(2J_i+1)}\,\frac{\Gamma_r^{d\to f}\Gamma_a^{d\to i}}{\Gamma_r^d+\Gamma_a^d}\,. \tag{3}$$

Here J_d and J_i are the total angular momenta of the intermediate and the initial-state ion, respectively. The Lorentzian line-shape function

$$L_d(E_{\text{c.m.}}) = \frac{\Gamma_d/(2\pi)}{(E_i+E_{\text{c.m.}}-E_d)^2+\Gamma_d^2/4}$$

is normalized to unity on the energy scale and $p = \sqrt{(E_{\text{c.m.}}/c)^2 + 2E_{\text{c.m.}}}$ in atomic units is the free-electron momentum associated with the kinetic energy $E_{\text{c.m.}}$. Here c denotes the velocity of light, E_i is the initial-level (ground-level) total energy of the Li-like Xe ion, and E_d is the total energy of the Be-like autoionizing level formed by dielectronic capture. Furthermore, Γ_d stands for the total natural width of the intermediate autoionizing level d, given as the sum of the radiative and autoionization widths: $\Gamma_d = \Gamma_r^d + \Gamma_a^d$. The radiative width is given as the sum over partial decay widths describing decays to different final levels f: $\Gamma_r^d = \sum_f \Gamma_r^{d\to f}$. We take into account electric dipole single-photon radiative decay channels, populating a multitude of final levels $1s^22p_{\bar{j}}n'l'_{j'}$ (with $2 \leqslant n' < n$) and $1s^22snl_j$. Since in the experiment the final levels of the ion are not resolved (e.g., the emitted photons are not detected), a summation over f is performed additionally Eq. (2).

The bound-state wave functions are obtained by means the multiconfiguration Dirac-Fock (MCDF) method, as implemented in the GRASP code [27,28]. In this scheme, a many-electron atomic state function (ASF) is given as a linear superposition of configuration state functions (CSFs) sharing common total angular momentum (J), magnetic (M), and parity (P) quantum numbers [27,28]:

$$|\gamma PJM\rangle = \sum_{k=1}^{n_c} c_k|\gamma_k PJM\rangle. \tag{4}$$

The CSFs $|\gamma_k PJM\rangle$ are constructed as jj-coupled N-particle Slater determinants of one-electron wave functions. In Eq. (4), γ_k is a multi-index that represents all quantum and occupation numbers needed to fully specify the CSF. The number of CSFs is denoted by n_c. γ collectively denotes all the γ_k included in the representation of the ASF. For the modeling of intermediate and final levels, we use configuration expansion sets constructed from the occupied orbitals in an average level scheme [27]. The initial Li-like ground level of the ion is described in the (single-configuration) Dirac-Fock approximation.

After the application of the MCDF method for solving the relativistic Coulomb problem, the Breit interaction correction is included by use of a configuration interaction method: matrix elements of the Breit interaction operator are calculated with wave functions generated by use of the self-consistent method with the Coulomb interaction added to the Dirac-Coulomb Hamiltonian matrix, and the resulting matrix is rediagonalized as in previous work [20].

The Auger width is given by

$$\begin{aligned}\Gamma_a^{d\to i} &= \frac{2\pi}{2J_d+1}\sum_{M_d}\sum_{M_i m_s}\int \sin(\theta)d\theta d\varphi \\ &\quad\times |\langle\Psi_d;J_dM_d|V_C+V_B|\Psi_iE_{\text{c.m.}};J_iM_i,\vec{p}m_s\rangle|^2 \\ &= 2\pi\sum_{\kappa_c}|\langle\Psi_d;J_d||V_C+V_B||\Psi_iE_{\text{c.m.}};J_ij_c;J_d\rangle|^2\,.\end{aligned}$$

In this equation, the matrix elements of the Coulomb and Breit interaction (V_C and V_B, respectively) are calculated with the initial bound-free product state i and the bound resonant intermediate state d. The total angular momentum of a partial wave of the continuum electron is given by j_c, while κ_c is the corresponding Dirac angular quantum number and $\vec{p}$ is the vectorial momentum of the free electron. After summation over the initial magnetic quantum numbers and integration over the direction (θ,φ) of the incoming continuum electron, and after performing the summation over the magnetic quantum number of the autoionizing state, one obtains the partial wave expansion in terms of the reduced matrix elements, as given in the last line of the above equation.

After the generation of the bound wave functions and mixing coefficients by use of the MCDF method, the radial continuum orbitals entering the Auger matrix elements are calculated numerically from a potential consisting of the nuclear potential and an additional screening potential induced by the frozen $1s^2\,2s$ inner-shell electrons. In the case of a heavy highly charged ion such as lithiumlike xenon the frozen-core assumption is expected to be a reliable approximation. The autoionization widths are calculated with coding similar to that used in Refs. [21,26].

III. EXPERIMENT

The experiment was performed using the accelerator and storage-ring facilities of the GSI Helmholtzzentrum für Schwerionenforschung (GSI) in Darmstadt, Germany. Li-like $^{136}\mathrm{Xe}^{51+}$ ions were stored in the Experimental Storage Ring (ESR) [29] at energies of 58.43 MeV/u and cooled applying electron cooling [30]. Typical stored-ion currents were 250 to 750 μA corresponding to 3×10^6 to 1×10^7 ions. The ESR is equipped with an electron cooler [31] which provides an electron beam with a narrow energy distribution mainly determined in the lateral directions by the cathode temperature $k_BT_\perp = 120$ meV and a temperature in longitudinal direction which is about three orders of magnitude lower, that is, $k_BT_\| \approx 0.2$ meV. The Xe^{51+} ion beam was cooled for several seconds, employing an electron current of 100 mA in order to reach equilibrium between cooling and intrabeam scattering and thus to ensure well-defined and optimal experimental conditions. Cooling adjusts the ion velocity to that of the electrons, leading to a vanishing collision energy $E_{\mathrm{c.m.}} = 0$. The second purpose of electron cooling is the reduction of the velocity spread of the ion beam to well below 10^{-4}. It is worth noting that after this initial cooling time essentially all Li-like ions are in their atomic ground states.

In the present experiment, the cooler electron beam was alternatingly switched for periods of a few tens of ms between electron cooling and an offset potential, thus introducing collision energies $E_{\mathrm{c.m.}} > 0$. This procedure, which is described in more detail in Sec. III A, ensured that ion beam energy and its momentum spread are maintained during the data taking. Experimental data were acquired for ~120 s, which is to be compared with a typical beam lifetime of ~200 s. Xe^{50+} recombination products from electron-ion collisions that occurred in the beam overlap region of the electron and ion beams are separated from the circulating Xe^{51+} primary beam ions in the ring dipole magnet following the electron cooler. A single-particle detector located in a detector pocket with a 25-μm steel entrance window was used to count the Xe^{50+} reactions products with practically 100% detection efficiency. From the count rate in dependence on the collision energies $E_{\mathrm{c.m.}}$ the DR resonance spectrum is inferred. By normalization of the number of recombined ions on the initial electron and ion beam intensities a merged-beams rate coefficient was determined on an absolute scale (Sec. III B).

A. Experimental collision energies

The variation of the electron energy in the cooler is performed with the aid of an additional potential U_{dt} that is applied to two drift tubes with a combined length of 1.94 m. The drift tubes are located in the beam overlap region (length $L = 2.5$ m) of the electron cooler. For a measurement step (M) at a collision energy $E_{\mathrm{c.m.}}$ in the center-of-mass (c.m.) frame, the drift tube potential U_{dt} was set to a corresponding value $U_{\mathrm{dt}}^{(\mathrm{M})}$ [see Eqs. (5) and (6)]. After a duration of ~32 ms, U_{dt} was switched back to cooling (C) condition $U_{\mathrm{dt}}^{(\mathrm{C})}$ for likewise ~32 ms. The two steps were repeated several hundred times with different measurement-step energies each time. The steps form a measurement cycle (ramp) that, in turn, was repeated many times in order to reduce statistical uncertainties. The individual measurement voltages of a ramp were chosen to produce a series of energy steps that were equidistant in the center-of-mass frame. The short measurement intervals and the intermittent cooling steps serve several purposes. The most important ones are as follows: The scheme prevents a change in the ion velocity due either to a cooling drag force towards the electron velocity at the measurement voltage or to energy loss in the residual gas (~10^{-11} mbar) of the storage ring. Furthermore, the heating of the ion beam from intrabeam scattering is compensated.

Swift and precise switching of the voltages up to ±5 kV with rise times of about 1 ms was accomplished with a set of eight individual power supplies that were toggled. A value of zero volt was obtained by means of a fast grounding switch. A description of the device can be found in Ref. [32]. Despite this effort, in each step the drift tubes reach the desired value only asymptotically. The actual value of the drift tube voltage was measured as a function of time by means of two different high-precision voltage dividers. In order to reach a voltage stability of the drift tubes of the order of 10^{-4}, the first 14 ms of each ~32-ms step were excluded from the data analysis. The stability of the voltage was also verified by checking the consistency and fixed values of the DR resonance positions for different experimental settings.

The relevant potentials for determination of the collision energy E_{lab} in the laboratory frame are (a) the constant (negative) cathode potential U_{cath}, (b) the drift tube voltage $U_{\mathrm{dt}}^{(C,M)}$, and (c) the (negative) space-charge potential $U_{\mathrm{sc}}^{(C,M)}$. With the electron rest mass m_{e0}, the relativistic Lorentz factor for the electrons γ_e can be determined as [4]

$$\gamma_e^{(C,M)} = 1 + \frac{E_{\mathrm{lab}}}{m_{e0}c^2} = 1 + \frac{e\left(|U_{\mathrm{cath}}| + U_{\mathrm{dt}}^{(C,M)} + U_{\mathrm{sc}}^{(C,M)}\right)}{m_{e0}c^2}\,. \tag{5}$$

From the definition of electron cooling, the electron beam (e) and the cooled ion beam (i) have identical velocities, that is, $\gamma_i^{(C)} \equiv \gamma_e^{(C)}$. The additional voltages of maximum ±5 kV that are applied to the drift tube do not significantly changed the energy (~58 MeV/u) of the circulating $^{136}\mathrm{Xe}^{51+}$ ions.

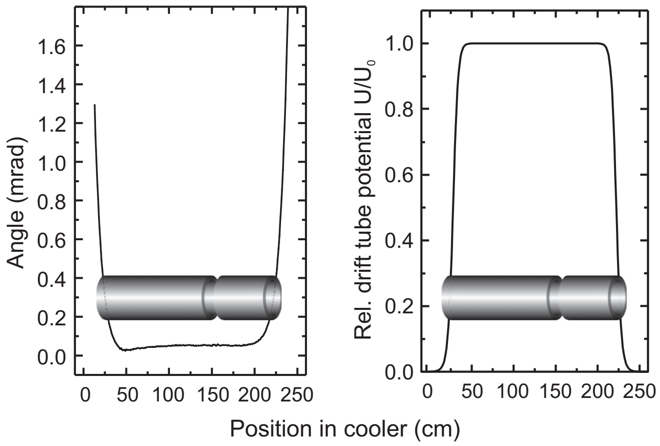

FIG. 1. Distribution of collision angles in the electron and ion beam overlap section of the electron cooler (left), and potential distribution of the drift tube used to accelerate or decelerate the electrons (right). The drift tubes are schematically shown as well. For details, see the text.

As a consequence, during measurement $\gamma_i^{(M)} \approx \gamma_i^{(C)}$ holds to a high precision as well. Once γ_i and γ_e are known, the relative collision energy $E_{\mathrm{c.m.}}$ in the center-of-mass frame can be calculated using [33]

$$E_{\mathrm{c.m.}} = m_{i0}c^2(1+\mu)\left[\sqrt{1+\frac{2\mu}{(1+\mu)^2}(\Gamma-1)}-1\right] \tag{6}$$

with ion rest mass m_{i0}, mass ratio $\mu = m_{e0}/m_{i0}$, and

$$\Gamma = \gamma_e\gamma_i - \sqrt{\left(\gamma_e^2-1\right)\left(\gamma_i^2-1\right)}\cos\vartheta.$$

The nominal angle ϑ between the merged electron and ion beams is zero, that is, $\cos\vartheta = 1$ with good accuracy for about 4/5th of the beam overlap (for details, see Sec. III C 2, and Fig. 1). The alignment of the beams was verified prior to the measurement by variation of the interaction angle and by minimizing the ion beam width using a beam profile monitor and Schottky diagnostics.

Two measurement modes depending on the wanted center-of-mass energy were applied: In our “*standard measurement mode*”, the cathode potential was set to its cooling value of $U_{\mathrm{cath}} = -32088$ V, corresponding to an ion energy of 58.43 MeV/u ($\beta_i = 0.3385$; $\gamma_i = 1.06273$). In this case, the available drift-tube potential variation of up to ±5 kV restricts the relative (center-of-mass) collision energy to $E_{\mathrm{c.m.}} < 206.2$ eV [see Eqs. (5) and (6)].

For higher collision energies, an “*extended measurement mode*” was used. In this mode, the cathode potential was set to $U_{\mathrm{cath}} = -36163$ V. Cooling was achieved by compensating this offset with a drift tube potential of $U_{\mathrm{dt}}^{(\mathrm{C})} = -4.1$ kV. In doing so, the ion energy remained unchanged. This was verified by monitoring the Schottky revolution frequency of the circulating ions. The resulting voltage range between cooling at $U_{\mathrm{dt}}^{(\mathrm{C})} = -4.1$ kV and the maximum positive voltage of +5 kV amounts to 9.1 kV, allowing for relative collision energies of up to $E_{\mathrm{c.m.}}^{(\max)} = 550$ eV.

U_{dt} as well as U_{cath} were stable to a few 10^{-4}. Other sources of uncertainties for the determination of collision energies arise from digitalization of the voltages (0.3 V) and the space-charge corrections $U_{\mathrm{sc}}^{(C,M)}$. These values yield relative uncertainties for $E_{\mathrm{c.m.}}$ between 3×10^{-4} and 1×10^{-3} at 550 and 10 eV, respectively. This initial energy determination is further improved by utilizing the regular Rydberg pattern of the DR resonances (see Sec. IV C).

B. Rate coefficient

The measured merged-beams rate coefficient $\alpha(v_{\mathrm{c.m.}})$ is a convolution of velocity and the cross section $\sigma(v)$ with the distribution of relative velocities of electrons and ions $f(v_{\mathrm{c.m.}},\vec{v})$:

$$\alpha(v_{\mathrm{c.m.}}) = \langle v\sigma(v)\rangle = \int \sigma(v)vf(v_{\mathrm{c.m.}},\vec{v})\,d^3v. \tag{7}$$

From the measured count rate R, normalized to ion current I_i, and electron density n_e, the recombination rate coefficient α is calculated as [20,34]

$$\alpha = \frac{1}{1-\beta_e\beta_i}\frac{qe\beta_i cR}{I_i n_e L}, \tag{8}$$

where ion and electron velocities $\beta_{i,e} = (1-1/\gamma_{i,e}^2)^{1/2}$ are given in units of the speed of light c, $q = 51$ is the initial ion charge state, e the electron charge, and $L = 2.5$ m the nominal length of the electron-ion merging region. It is worth emphasizing that for most early merged-beams DR experiments at low relative collision energies (that is, for $\beta_i \approx \beta_e$), the term $1/(1-\beta_e\beta_i)$ was approximated by γ_i^2 [34]. For significantly different velocities of electrons and ions as, for example, in Ref. [20], this approximation is invalid and Eq. (8) has to be used.

The systematic uncertainty of the rate coefficient $\Delta\alpha$ is mainly caused by the uncertainties of the electron density $\Delta n_e/n_e = 10\%$, the ion current $\Delta I_i/I_i = 7\%$, the detector efficiency $\Delta R/R = 5\%$, and the corrections with respect to the response function of 5%. The square sum of all individual contributions results in a 14% uncertainty of the rate coefficient. Background substraction (see Sec. III D) causes an additional uncertainty of up to 10% for the DR resonance strengths extracted from the spectrum. In total, for the DR rate coefficient and the DR resonance strengths, a systematic uncertainty of 17% results. In comparison, the typical statistical uncertainties are significantly smaller.

C. Experimental response function

The measured merged-beams recombination rate coefficient depends on the atomic recombination cross section and on the experimental response function $f(v_{\mathrm{c.m.}},\vec{v})$, see Eq. (7). Thus, a meaningful comparison between a measured DR spectrum and a theoretical prediction has to take into account the experimental conditions on a reasonably detailed level. For the present experiment, $f(v_{\mathrm{c.m.}},\vec{v})$ is mainly determined by three contributions: first, a flattened Maxwell-Boltzmann distribution that describes the thermal velocities of the electrons. In addition, the merging and demerging sections of the beams and the actual mapping of the magnetic guiding field of the electron beam lead to a distribution of nonzero interaction angles. Finally, the distribution of potentials of the set of drift tubes that is used to accelerate or decelerate the electron beam has to be accounted for.

1. Thermal velocity distribution of the electrons

The experimental energy resolution is mainly determined by the relative spread of the electron-ion relative velocity. For an electron-cooled ion beam the contribution from the ion beam is typically significantly smaller and can be neglected in most cases [16] (for an exception, refer to Ref. [20]). The electron beam is commonly described by a flattened Maxwellian distribution around the average velocity v_0, and is characterized by the two temperatures $k_BT_\perp$ and $k_BT_\parallel$ with $k_BT_\parallel \ll k_BT_\perp$ [30]:

$$f(v_0,\vec{v}) = \sqrt{\frac{m_{e0}}{2\pi k_BT_\parallel}}\exp\left[-\frac{m_{e0}(v_\parallel - v_0)^2}{2k_BT_\parallel}\right] \times \frac{m_{e0}}{2\pi k_BT_\perp}\exp\left[-\frac{m_{e0}v_\perp^2}{2k_BT_\perp}\right]. \quad (9)$$

Both temperatures determine the experimental electron-ion collision energy spread $\Delta\tilde{E}_{\mathrm{c.m.}}$ (full width at half maximum) [35]

$$\Delta\tilde{E}_{\mathrm{c.m.}}(E_{\mathrm{c.m.}}) = \sqrt{[k_BT_\perp \ln(2)]^2 + 16\ln(2)k_BT_\parallel E_{\mathrm{c.m.}}}. \quad (10)$$

For low electron-ion collision energies, $\Delta\tilde{E}_{\mathrm{c.m.}}$ is mainly determined by the transversal temperature $T_\perp$. Additionally, $T_\perp$ introduces an energy-independent asymmetry and a shift of the center of gravity by about $k_BT_\perp$ towards lower collision energies. $k_BT_\parallel$ leads to an additional energy-dependent symmetric broadening which at higher energies results in a symmetric but still shifted resonance.

From the measured widths and shapes of resonances at different energies the electron beam temperatures were extracted. The results of this analysis for the present measurement are $k_BT_\parallel \approx 200$ μeV and $k_BT_\perp \approx 120$ meV. These values are comparable to the parameters of earlier DR merged-beams experiments at the ESR [4,36] and are used throughout the rest of the paper for the parametrizations of the response functions.

2. Spatial variation of the B-field inside the electron cooler and potential distribution of the drift tube

The electrons in the cooler follow the longitudinal magnetic guiding field of $B = 500$ G. In the toroid sections where electron and ion beams are merged and demerged, electrons and ions interact at an angle that distinctively differs from zero. Thus, from a total beam overlap length of 2.5 m electrons and ions are parallel roughly over a distance of 1.7–2.0 m (see Fig. 1). In addition, the solenoid field in the main part of the beam overlap is collinear with the ion beam axis within a few 10^{-2} mrad even with corrections applied. Both contributions introduce changes to the response function $f(v_{\mathrm{c.m.}},\vec{v})$. The actual field mapping (see Fig. 1, left panel) is taken into account in a Monte Carlo (MC) simulation (see Sec. III C 3). The simulation uses only the deviations from an average angle of zero, thus reflecting the efforts that during the initial preparation of the experiment in the storage ring a minimum average interaction angle is set up.

A further contribution that enters the response function stems from the drift tubes used to vary the electron energy. The potential distribution on axis $r = 0$ between drift tubes at potential V_{DT} and with radius b, and additional adjacent cylindrical electrodes V_{CE} with the same radius can be approximated by [37]

$$V(r = 0,z) = \frac{V_{\mathrm{CE}} + V_{\mathrm{DT}}}{2} + \frac{V_{\mathrm{DT}} - V_{\mathrm{CE}}}{2}\tanh\left(\frac{1.318\,z}{b}\right), \quad (11)$$

where the point $z = 0$ is located at the edge of the drift tube. Outside the drift tubes of length $L = 1.94$ m the potential is 0 V. The right panel in Fig. 1 depicts the potential distribution for the drift tubes of the ESR electron cooler.

3. Monte Carlo simulations

In order to simulate a merged-beams rate coefficient spectrum α_{sim} on the basis of a given theoretical cross section and the response function $f(v_{\mathrm{c.m.}},\vec{v}')$, a MC simulation program was developed [36].

For the MC response function a pair of relativistic 4-momentum vectors $\mathcal{P}_{i,e} = (\mathcal{E}_{i,e}/c;\vec{p}_{i,e})$ for each of the collision partners, electrons, and ions was set up. Such a pair of 4-vectors defines a collision event. Here $\mathcal{E} = E + m_0c^2$ the total energy, E is the kinetic energy, and $\vec{p}$ is the momentum vector of the electron (e) and the ion (i). For a given collision energy $E_{\mathrm{c.m.}}$, that is, for a given measurement step at a set value E_s, the nominal value for the drift tube voltage was calculated from ion energy and cathode voltage. With additional input parameters for ion momentum spread $\delta p/p$, for ion beam emittance or the ion beam temperatures, and the electron beam temperatures $T_\perp$ and $T_\parallel$ (see Sec. III C 1) the according distributions were randomly sampled, and the 2×4 components of a Monte Carlo pair $\mathcal{P}'_{i,e}$ are filled. In addition, the 2.5-m beam overlap region is discretized and a position $z^{(k)} \in [0,2.5$ m$]$ is likewise randomly generated. From this position an interaction angle as given from the magnetic field mapping and an actual potential value along the drift tube (see Sec. III C 2) are chosen and are included in the corresponding momentum vector components. The full 4-momentum vector of a Monte Carlo collision event (indicated by primed variables) in the laboratory frame is $\mathcal{P}'_{\mathrm{lab}} = (\frac{\mathcal{E}'_e+\mathcal{E}'_i}{c};\vec{p}'_e + \vec{p}'_i,)$ for each collision event. Using the Lorentz invariance $\mathcal{P}^2_{\mathrm{lab}} = \mathcal{P}^2_{\mathrm{c.m.}}$ and the definition $\mathcal{P}_{\mathrm{c.m.}} = (\frac{\mathcal{E}_{\mathrm{c.m.}}}{c};0)$ for the center-of-mass frame, E' or v' of the Monte Carlo event in the center-of-mass frame are readily calculated and are used for a numerical convolution with the cross section. For a given set value E_s the procedure is repeated up to a few hundred thousand times until the outcome is no longer biased by the Monte Carlo statistics. In the same manner, further energy E_s steps are simulated until completion of a full spectrum.

Figure 2 shows a Monte Carlo simulation of the response function $f(E',E)$ for settings at a nominal collision energy $E_s = 10$ eV, that is, $U_{\mathrm{cath}} = 32.088$ kV and $U^{(m)}_{\mathrm{dt}} = 1161.21$ V. For the simplified assumption of δ-like DR resonances, a

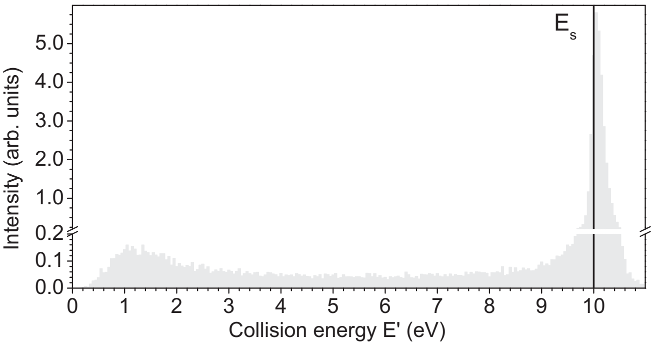

FIG. 2. Simulated Monte Carlo response function $f(E',E_s)$ for a set energy value in the center-of-mass frame of $E_s = 10$ eV (black line) for a cathode potential $U_{\text{cath}} = 32.088$ kV and a corresponding drift tube voltage $U_{\text{dt}}^{(M)} = 1161.21$ V. The temperatures $k_B T_\perp = 120$ meV and $k_B T_\parallel = 200$ meV were used. Please note the axis break and the according different scales used to emphasize details of the response function.

convolution with $f(E',E_{\text{c.m.}})$ for the full range of set energy values of a given range leads to a simulated rate coefficient spectrum $\alpha_{\text{DR}}(E_{\text{DR}},E_{\text{c.m.}})$, as shown in Fig. 3. As detailed in Sec. III C 1, $\alpha_{\text{DR}}(E_{\text{DR}},E_{\text{c.m.}})$ is broadened and shifted to lower collision energies caused by the $T_\parallel$ and $T_\perp$ of the electron beam, respectively. The shape of the main part of the resonance is nearly unaffected by the drift tube effects and angle variations and is still determined by $T_\parallel$ and $T_\perp$. In addition, a tail and a pedestal on the higher-energy side of the resonance are visible that are caused by the slope of the potential at the edge of the drift tubes, that is, the resonance at $E_{\text{c.m.}} = 10$ eV still contributes to α_{DR}, for example, at $E_{\text{c.m.}} = 11$ eV, due to the lower voltages. The corresponding smooth background increases with every new DR resonance. Contributions outside the drift tube on potential close to 0 V are suppressed since the interaction angle increases as a consequence of merging and demerging in the toroid sections (compare Fig. 1).

Since the drift tubes are only about four-fifths of the full overlap length $L = 2.5$ m [see Eq. (8)] and due to the "leakage" of resonance strength into pedestal and background, the measured apparent resonance strength is significantly lower than the one from a convolution of the DR cross section with the anisotropic Maxwell-Boltzmann distribution [Eq. (9)], cf. Fig. 3. For small drift tube voltages $U_{\text{dt}} \approx 0$ nearly the full overlap length of 2.5 m is on the desired potential, but the merging and demerging result in an apparent resonance strength of about 94% of the real one. For higher U_{dt}, this ratio rapidly decreases to about 0.55–0.6 depending on the actual settings. All spectra shown in this paper are corrected for this apparent resonance strength.

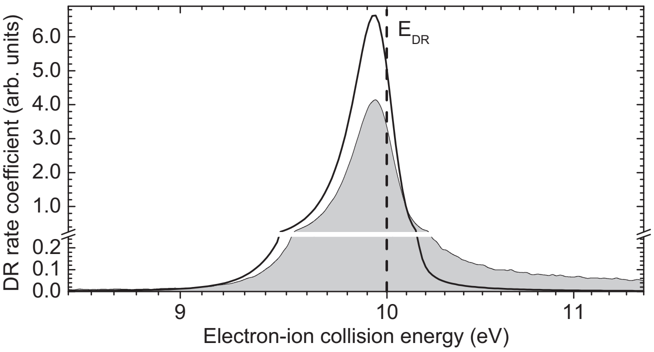

FIG. 3. Rate coefficients of a synthetic DR resonance at $E_{\text{DR}} = 10$ eV (vertical line). Displayed are the rate coefficient as obtained from a convolution with the anisotropic Maxwellian velocity distribution [Eq. (9)] with $k_B T_\parallel = 200$ μeV and $k_B T_\perp = 120$ meV (black line) and the rate coefficient from a full Monte Carlo simulation (gray area). Please note the axis break and the according different scales.

D. Background processes

The process of photorecombination (PR) consists of the direct channel, radiative recombination (RR), and the resonant channel, dielectronic recombination (DR). In the present study, the smooth nonresonant contribution due to RR is treated as a background and is subtracted from the data: The following semiclassical cross section for RR into hydrogenic states with quantum number n has been given by Bethe and Salpeter [38,39]:

$$\sigma_{\text{RR}}^{(n)}(E_{\text{c.m.}}) = 2.1 \times 10^{-22}\text{cm}^2 \times \frac{\left(Z_{\text{eff}}^2 \text{R}_\infty\right)^2}{n E_{\text{c.m.}} \left(Z_{\text{eff}}^2 \text{R}_\infty + n^2 E_{\text{c.m.}}\right)}.$$

Here $R_\infty = 13.6057$ eV is the Rydberg energy and Z_{eff} is the effective charge state. The total RR cross section σ_{RR} is the sum over the partial cross sections $\sigma_{\text{RR}}^{(n)}$ of all available final principal quantum numbers n up to maximum cut-off n_{max} defined by the highest Rydberg state that survives field ionization in the ring dipole magnets [40]. In addition, the unoccupied fraction of each shell is taken into account. Gaunt factors [39] are applied as a correction of the semiclassical cross section towards the quantum-mechanical calculation of Stobbe [41]. For background subtraction of the RR contribution, the RR rate coefficient $\alpha_{\text{RR}}^{\text{sim}}$ is included in our Monte Carlo code.

For the measured rate coefficient there is an additional background α_{bg} caused by collisions between ions and residual gas atoms. The additional background contribution α_{bg} not caused by RR is fitted with a linear function and is also subtracted from the data.

IV. RESULTS AND DISCUSSION

In this section we present the results of our $^{136}\text{Xe}^{51+}(2s) + \text{e}^- \rightarrow {}^{136}\text{Xe}^{50+}\,(2p_{1/2,3/2}\; nl_j)_J$ recombination experiment. Section IV A provides an overview and a first discussion of the bulk features of the DR resonance pattern. In Sec. IV B, a closer look at the fine structure within the individual $2p_{\bar{j}}nl_j$ Rydberg peaks is given and a comparison between the measured spectrum and our MCDF calculations is performed. Based on the regular structure of the DR resonance series, an improved energy calibration is obtained (see Sec. IV C) that is used in Sec. IV D to determine the $2s \rightarrow 2p_{1/2}$ and $2s \rightarrow 2p_{3/2}$ excitation energies. From the experimental spectra, DR resonance strengths of fully resolved resonance groups are extracted and are compared to MCDF calculations (Sec. IV E).

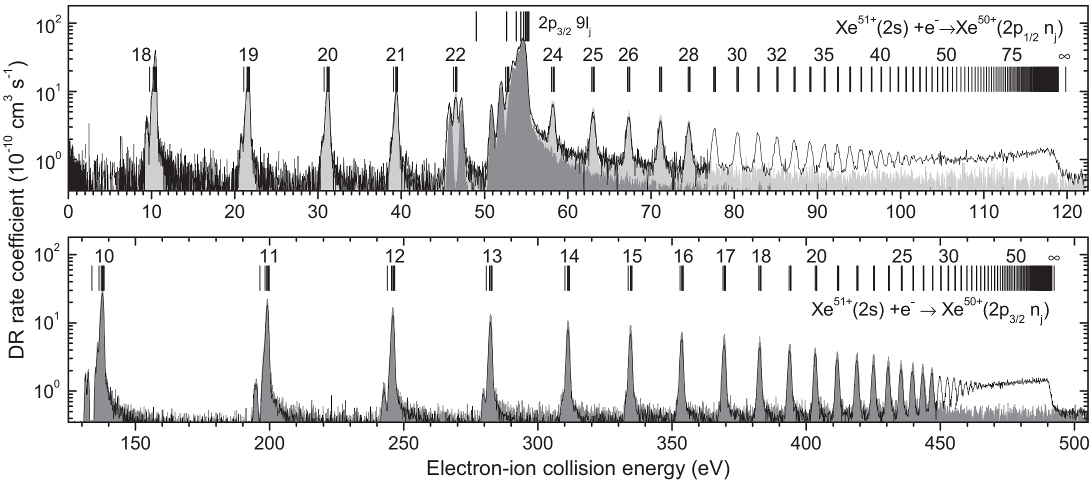

FIG. 4. Measured $^{136}Xe^{51+}$ DR spectrum (black line) after substraction of residual gas and RR background. Resonance energies, using the excitation energies $E_{ex}(2s \rightarrow 2p_{1/2}) = 119.820$ eV from Ref. [9] and $E_{ex}(2s \rightarrow 2p_{1/2}) = 492.4$ eV from Ref. [10] and hydrogen-like Dirac binding energies [Eq. (13)], are indicated by two sets of vertical bars. The shaded areas are the results of our MCDF calculations for $Xe^{51+}(2s) + e^- \rightarrow Xe^{50+}(2p_{1/2}\ nl_j)_J$ (light gray) and $Xe^{50+}\ (2p_{3/2}\ nl_j)_J$ (dark gray) and cover DR Rydberg resonances for n up to 28. The MCDF energies are shifted by the same values -0.47 and -0.345 eV for each of the $2p_{1/2}nl_j$ and $2p_{3/2}nl_j$ resonances, respectively. The calculated cross sections have been convoluted with the experimental response functions (see Sec. III C 3).

A. DR spectrum of $^{136}\mathbf{Xe}^{51+}$: overview

In the investigated electron-ion collision energy range between 0 and 505 eV, $\Delta n = 0$ DR resonances of the two Rydberg series $^{136}Xe^{51+}(2s) + e^- \rightarrow Xe^{50+}\ (2p_{1/2}\ nl_j)_J$ and $Xe^{50+}\ (2p_{3/2}\ nl_j)_J$ are located (see Fig. 4). The data are presented as a DR-only rate coefficient, that is, after background subtraction (Sec. III D). These resonances are associated with the excitations $E_{ex}(2s \rightarrow 2p_{1/2}) = 119.820(8)$ eV [9] and $E_{ex}(2s \rightarrow 2p_{3/2}) = 492.4(6)$ eV [10], respectively. The resonance energies are given according to

$$E_{DR}(\bar{j}, nl_j) = E_{ex}(2s \rightarrow 2p_{\bar{j}}) - E_B(nl_j), \qquad (12)$$

where E_{DR} is the DR resonance energy and $E_B(nl_j)$ the binding energy of the Rydberg electron. The spectra show a complex fine structure within a Rydberg peak. As a consequence, on the present level of precision a plain Rydberg formula $R_\infty Z^2/n^2$ for the binding energy as used in many of the earlier DR experiments is inadequate for an accurate description. An improvement is achieved [21] by approximation of $E_B(nl_j)$ with Dirac binding energies for hydrogen-like ions,

$$E_{nj}^{\mathrm{Dirac}} = m_{e0}c^2 / \sqrt{1 + \left(\frac{Z\alpha}{n - K + \sqrt{K^2 - (Z\alpha)^2}} \right)^2} - m_{e0}c^2, \qquad (13)$$

with $K = j + 1/2$ and $\alpha \approx 1/137$ the fine-structure constant. The Dirac binding energy includes the fine structure of the Rydberg electron. For Li-like ions an effective nuclear charge $Z_{\mathrm{eff}} = Z - 3$ is employed, that is, the nuclear charge reduced by the charge of the three core electrons.

As shown in Fig. 4 (vertical bars), the resonance positions within the DR spectrum are well described in this approximation, in particular for high angular momenta j of the Rydberg electron. The Dirac-based description, however, neglects the mutual electron-electron interaction of Rydberg and core electrons (compare Figs. 5 and 6). In a classical picture, Rydberg electrons with high angular momentum j do not penetrate the Li-like electron core, thus the approximation is best for the highest values of j. For low angular momenta j, the Rydberg electron has a significant probability density inside the cloud of the three inner-shell electrons. For lower j, the fine-structure splitting in Li-like ions is larger than the Dirac approximation with a Z_{eff} and tends towards the one for the unshielded nucleus Z. This behavior is also directly revealed in our spectra (see Figs. 5 and 6). The main resonance strength within an n-Rydberg-manifold is cumulated in the unresolved bulk peak consisting of high-angular-momentum resonances. A more detailed investigation of these high-total-angular-momentum contributions and their impact on the determination of the underlying excitation energies can be found in Refs. [4,21,42].

In our experimental spectra, individual Rydberg resonances are resolved up to $n = 43$ for DR associated with $2s \rightarrow 2p_{1/2}$ excitations and up to $n = 36$ for the $2p_{3/2}$ series. Contributions from higher nonresolved Rydberg states are visible up to energies close to the series limits $E_B(n \rightarrow \infty) \equiv E_{ex}$. Weakly bound electrons in high-Rydberg states can be reionized by field ionization in the motional electric $\vec{v}_i \times \vec{B}$ fields of the magnets of the storage ring before they reach the particle detector [40]. Due to the high charge state of Xe^{51+}, this takes place only for principal quantum numbers above $n \sim 110$. Thus, in contrast to storage-ring DR measurements with lighter ions (compare, for example, Ref. [40]), in Xe^{51+} this field ionization has only a minor effect on the measured DR rate coefficient at the series limit.

B. DR spectrum: Details of fine structure and comparison with MCDF calculations

Explicit MCDF calculations for DR of Xe^{51+} were carried out up to the principle quantum number $n = 28$. The

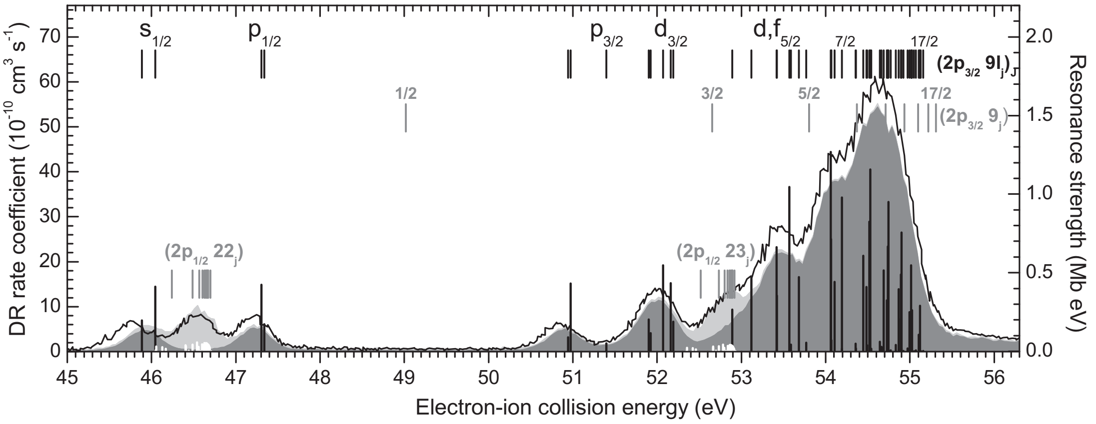

FIG. 5. Measured $^{136}\mathrm{Xe}^{51+}$ DR spectrum in the energy range of the $2s + e^- \rightarrow (2p_{3/2}\,9l_j)_J$ resonance group (black line) in comparison with our MCDF calculation for the $(2p_{3/2}\;9\mathrm{l}_j)_J$ resonance group (dark shaded areas) and for the $n = 22$ and $n = 23$ groups of the $2p_{1/2}\;nl_j$ Rydberg resonance series (light shaded areas) shifted by -0.345 eV and -0.47 eV, respectively. The theoretical cross sections have been convoluted with the Monte Carlo response function (see Sec. III C 3). Corresponding resonance strengths and (shifted) energies from our MCDF calculations are given by black and white vertical lines for $(2p_{3/2}\;9\mathrm{l}_j)_J$ and $(2p_{1/2}\;nl_j)_J$ resonances, respectively. The vertical bars indicate resonance positions from the energy-shifted MCDF theory (black) and from the hydrogenlike (Dirac) approximation (gray). The later are calculated according to Eqs. (12) and (13) with measured $2s \rightarrow 2p_j$ excitation energies from Refs. [9,10].

theoretical cross sections were convoluted with the experimental response function (see Sec. III C 3) and are given as shaded areas in Figs. 4 to 6. Contributions of the $(2p_{1/2}\;nl_j)_J$ and $(2p_{3/2}\;nl_j)_J$ resonance manifolds are distinguished by light and dark gray shading.

The lowest n into which the dielectronic capture (DC) can proceed are $n_{\min} = 18$ and $n_{\min} = 9$ for $2s \rightarrow 2p_{1/2}$ and for $2s \rightarrow 2p_{3/2}$ excitations, respectively. Doubly excited states with lower principle quantum numbers are below the autoionization threshold and, consequently, a DC is energetically forbidden. Figures 5 and 6 present enlarged views of the respective lowest-energy resonance manifolds $(2p_{1/2}\;18l_j)_J$ and $(2p_{3/2}\;9l_j)_J$. As a consequence of the high Z, the fine-structure intervals are strongly magnified. In combination with our high experimental energy resolution, for many of the high-n Rydberg states the fine structure was partly resolved, thus allowing for a detailed comparison with calculations and a state-resolved extraction of DR resonance strengths from the measured data (Tables IV and V).

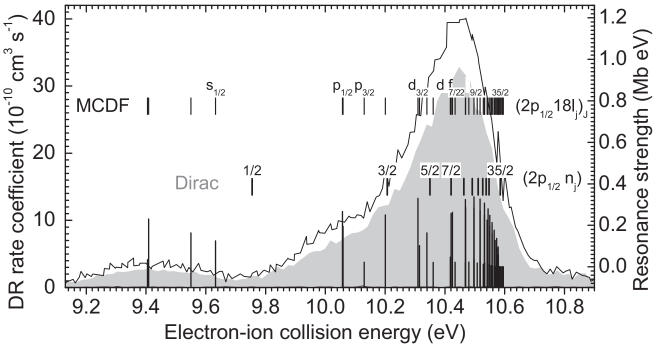

FIG. 6. $^{136}\mathrm{Xe}^{51+}$ DR spectrum in the energy range of the $2s + e^- \rightarrow (2p_{1/2}\;18l_j)_J$ resonance group. The experimental results (black line) are compared with the result of the MCDF calculation (light shaded area). The theoretical energy scale is shifted by -0.47 eV and the theoretical cross section has been convoluted with the experimental response function (see Sec. III C 3). Theoretical resonance strengths and (shifted) energies are given by black vertical lines. Black and gray vertical bars indicate resonance positions from the energy-shifted MCDF theory and from $2s \rightarrow 2p_{1/2}$ excitation energy [9] combined with hydrogen-like approximated binding energies, respectively.

For a better comparison with the experimental data, the whole theoretical MCDF Rydberg patterns $(2p_{1/2}\;nl_j)_J$ and $(2p_{3/2}\;nl_j)_J$ were shifted by -0.47 and -0.345 eV, respectively. The calculated DR cross sections were slightly adjusted to the shifted energies, thereby taking into account the p_{DR}^{-2} scaling of the resonance strengths, see Eq. (3). This energy shift of a Rydberg series as a whole is significantly higher than the experimental energy uncertainty after our improved energy calibration (see Sec. IV C). It can be attributed due mainly to an incomplete incorporation of QED and correlation contributions to the $2s$-$2p_{\bar{j}}$ energy splitting (see also Sec. IV D). Theoretical and experimental rate coefficients are on independent absolute scales. The experimental rate coefficients tend to be by a constant factor of ~15% smaller than the calculated ones. The factor is just at the edge of our 1σ systematic uncertainty for the DR rate coefficient. Beyond this common scaling factor and the overall small energy shifts, the MCDF calculations describe the structure and strengths of the resonance peaks very well. Unfortunately, the two $(2p_{3/2}\;9s_{1/2})_J$ resonances at around 46 eV are an exception to this behavior and are shifted by a few tenths of an eV towards higher energies with respect to the rest of the $(2p_{3/2}\;9l_j)_J$ manifold. Please note that already the $(2p_{3/2}\,9p_{1/2})_J$ resonances match perfectly. The reason for this deviation is not yet explained.

In Figs. 5 and 6, fine-structure energies are indicated as obtained from our MCDF calculations and, for comparison, from relativistic hydrogen-like binding energies with $Z_{\mathrm{eff}} = Z - 3 = 51$, Eq. (13). The excitation energies used in the figures are $E_{\mathrm{ex}}(2s \rightarrow 2p_{\bar{j}}) = 119.820(8)$ eV [9] and

$E_{\mathrm{ex}}(2s \to 2p_{\bar{j}}) = 492.4(6)$ eV [10]. In comparison to the one-electron description, the electron-electron interaction introduces an additional splitting within a given j group and a shift of such a j ensemble towards lower energies. As is expected from our naive classical picture above, this behavior is most pronounced for $j = 1/2$ and $j = 3/2$ and decreases significantly for higher j.

C. Improvement of the energy calibration

After the initial calibration of the energy scale from the measured voltages [Eqs. (5) and (6)] a further significant improvement of the energy calibration was achieved by utilization of the well-known regular Rydberg pattern of the DR process [compare Eq. (1) and Sec. IV]. The idea is similarly applied in some early work about DR, e.g., in Ref. [43] and was fully exploited by Brandau *et al.* [4]. For the present experiment the latter approach is slightly modified.

As discussed in Secs. IV A and IV B the energies of high-j DR resonances within a Rydberg manifold are given to a good approximation within a hydrogen-like Dirac description. Based on these considerations, the differences of the half-height position of the high-energy tails $E_{1/2}(\bar{j},n)$ and therefore the high-j components of the Rydberg resonances are used as an experimental measure for differences in the Rydberg binding energies. According to Eq. (13) for a given Z and j, the intervals between different n have fixed energy spacings which are used for an improvement of the energy calibration.

In order to address the energy dependence of the experimental response function (see Sec. III C), our Monte Carlo simulation has been used to include its leading aspects. For the half-height peak positions $E_{1/2}(\bar{j},n)$ the according corrections amount to an energy shift of $E_{\to}(E_{1/2}) = d(E_{1/2})^e$ with $d = (12.4 \pm 0.2)$ meV and $e = (0.598 \pm 0.004)$ for the present experiment yielding corrected half-height positions ${}_{1/2}E_{\mathrm{DR}}(\bar{j},n) = E_{1/2}(\bar{j},n) - E_{\to}[E_{1/2}(\bar{j},n)]$.

From the experimental and theoretical differences in Rydberg energies we obtain the conditions

$$\begin{aligned}&[{}_{1/2}E_{\mathrm{DR}}(\bar{j},n_{(i)}) - {}_{1/2}E_{\mathrm{DR}}(\bar{j},n_{(k)})]\\ &\quad \overset{!}{=} \left[E_{nj}^{\mathrm{Dirac}}\left(n_{(i)},j_{\max}^{(i)}\right) - E_{nj}^{\mathrm{Dirac}}\left(n_{(k)},j_{\max}^{(k)}\right)\right], \qquad (14)\end{aligned}$$

with E_{nj}^{Dirac} from Eq. (13). It is worth noting that a detailed knowledge of the resonance strength distribution within the high-energy tail of the Rydberg peaks is not required since only differences in their half-height positions and the differences in the $j_{\max}$ Dirac binding energies are used. In order to further minimize a potential bias, in our recalibration of the energy scale only pairs of Rydberg peaks are used that differ in principal quantum number by $|n_{(i)} - n_{(k)}| \leqslant 4$. For these neighboring Rydberg peaks any change of the resonance strength distributions is small [21]. For the present experiment this has also been verified in a self-consistent manner by comparison with pairs with larger Δn.

The calibration was parameterized as a linear dependency (factor and offset) on the measured drift tube voltage U_{dt}. Slightly different calibration values were used for the two measurement modes (Sec. III A). The recalibration of the drift tube voltages changed the values by less than 1% with remaining relative uncertainties for the voltages $<10^{-4}$. The calibration was carried out with the combined data of the present experiment with Li-like Xe^{51+} and a second experiment with Be-like Xe^{50+} [44] that used identical settings. Figure 7 shows the residua after the calibration versus the energy of the lower of the two resonances. The standard deviation of the residua is taken as the energy uncertainty $\Delta E_{\mathrm{c.m.}}$ of the revised energy scale $E_{\mathrm{c.m.}}$,

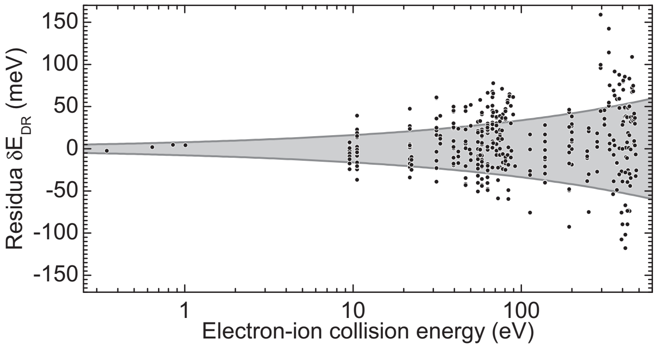

FIG. 7. ● Residua E_{res} (see text) versus calibrated energy $E_{\mathrm{c.m.}}$. The extracted energy-dependent 1σ energy uncertainty [Eq. (15)] is indicated as a gray area. The calibration was carried out with the combined data of the present experiment with Li-like Xe^{51+} and a second experiment with Be-like Xe^{50+} [44] that used identical settings.

$$\Delta E_{\mathrm{c.m.}} = \pm 7.8\ \mathrm{meV} \left(\frac{E_{\mathrm{c.m.}}}{\mathrm{eV}}\right)^{0.32}. \qquad (15)$$

The result is displayed in Fig. 7 and yields approximately $\Delta E_{\mathrm{c.m.}} = 16$ meV at $E_{\mathrm{c.m.}} = 10$ eV and $\Delta E_{\mathrm{c.m.}} = 57$ meV at $E_{\mathrm{c.m.}} = 500$ eV.

An additional major source of error in the determination of DR resonance positions arises from uncertainties of transversal $T_\perp$ and longitudinal $T_\parallel$ electron beam temperatures. $k_B T_\perp$ and $k_B T_\parallel$ were determined to 120^{+40}_{-20} meV and (200 ± 50) μeV, respectively. The unknown temperature contributes to the uncertainty of DR resonance positions $\Delta E_{\mathrm{DR}}(\Delta T_{\parallel,\perp})$ with

$$\frac{\Delta E_{\mathrm{DR}}(\Delta T_{\parallel,\perp})}{\mathrm{meV}} = 5.67 \times \ln\left(\frac{E_{\mathrm{DR}}}{\mathrm{eV}}\right) + 11.9. \qquad (16)$$

D. Excitation energies

Two basic approaches to determine the excitation energy by means of DR collision spectroscopy can be found in the literature: The first is based on the measurement of the energy of well-resolved DR resonances at very low collision energies [3,15] and the calculation of the Rydberg binding energies. The second method employs an extrapolation of the series of Rydberg resonances to the series limit $n \to \infty$ [4].

Our present approach is a hybrid of these two methods. In Sec. IV C we have already described how to utilize the Rydberg pattern for an improved calibration of the energy axis. Based on this initial work we deduct the excitation energies $E_{\mathrm{ex}}(2s \to 2p_{\bar{j}})$ from the $(2p_{1/2}18l_j)_J$ resonances between 9 and 11 eV (see Fig. 6) and from the $(2p_{3/2}9l_j)_J$ group between 45 and 56 eV (see Fig. 5). Both multitudes are the lowest DR-resonance groups associated with the $2s \to 2p_{1/2}$ and $2s \to 2p_{3/2}$ excitations, respectively. The inclusion of higher-n

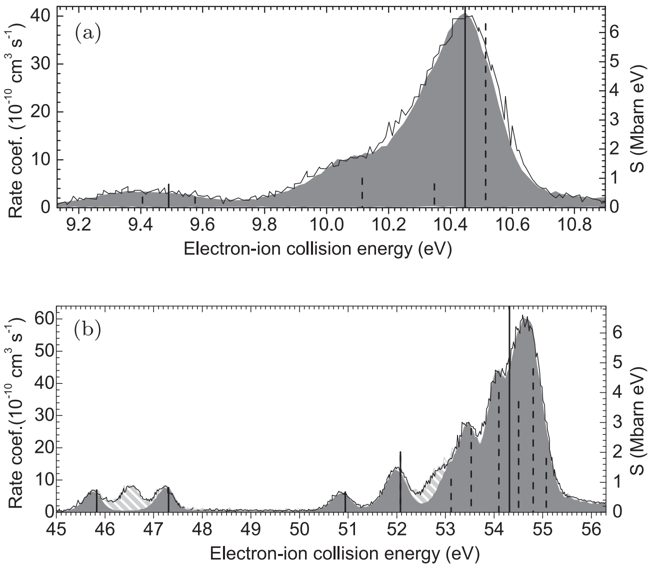

FIG. 8. Measured DR spectrum (solid line), fitted synthetic DR spectrum (gray area), and corresponding artificial resonance energies $E_{\mathrm{DR},i}$ and resonance strengths S_i (dashed bars). Full bars represent the average energies $\bar{E}_{\mathrm{DR}}$ (see text and Table I) and strengths $S = \sum_i S_i$. (a) $2s + e^- \to (2p_{1/2}18l_j)_J$ resonance group. (b) $2s + e^- \to (2p_{3/2}9l_j)_J$ resonance group. The hatched areas belong to the $2p_{1/2}\,n$ resonance series.

resonances does not further improve the result. For each of the two resonance manifolds we created a simplified synthetic spectrum consisting only of a few "toy" resonances (Fig. 8). The number i, the energies $E_{\mathrm{DR},i}$, and the resonance strengths S_i of these artificial resonances were chosen and fitted applying our Monte Carlo code such that all structures in the measured spectrum were fully reproduced. The synthetic resonances i (dashed bars) were averaged $\bar{E}_{\mathrm{DR}} = (\sum_i E_{\mathrm{DR,i}} S_i)/(\sum_i S_i)$ for fully resolved peaks (full bars). For the $(2p_{1/2}18l_j)_J$ group we distinguish two fully resolved peaks and for the $(2p_{3/2}9l_j)_J$ manifold five, respectively.

Initially, we intended to use Rydberg binding energies E_B as calculated directly with our MCDF code but it turned out that this approach is numerically not stable enough since MCDF resonance energies are determined from differences of the large total energies of initial and intermediate state. This introduced a significant scatter of a few tenths of an eV between individual calculations and would have lead to corresponding uncertainties for E_B. Still, the MCDF calculations describe the strengths and the overall shape of a resonance very well. Thus, we use the MCDF calculations to relate the measured resonance position to the energy of maximum angular momentum $j_{\max}$ state within each group and then calculate their binding energy from the exact Dirac energies $E_{nj}^{\mathrm{Dirac}}(n, j_{\max})$:

$$E_{\mathrm{ex}} = \bar{E}_{\mathrm{DR}} + E_{\mathrm{DR},\,j_{\max}}^{\rightarrow} + E_{n,\,j_{\max}}^{\mathrm{Dirac}},$$

where $E_{\mathrm{DR},\,j_{\max}}^{\rightarrow}$ is the according energy shift from full MCDF calculations to $j_{\max}$. The results of this procedure are presented in Table I for each considered resonance group.

The uncertainty in DR resonance positions $\Delta\bar{E}_{\mathrm{DR}}$ is dominated by the systematic uncertainties from the calibration of the energy axis [Eq. (15)] and from the electron beam temperatures [Eq. (16)]. The model uncertainty, that is, the shape and distribution of resonance strengths as well as the according mapping to a hydrogen-like (Dirac) description that enters the determination of the energy shift $E_{\mathrm{DR},\,j_{\max}}^{\rightarrow}$ were evaluated in detail within the scope of earlier measurements [4,21]. For $\Delta E_{\mathrm{DR},\,j_{\max}}^{\rightarrow}$ we obtain an upper estimate of 30 meV.

TABLE I. Determination of excitation energies E_{ex} from measured averaged resonance position $\bar{E}_{\mathrm{DR}}$, energy shift $E_{\mathrm{DR},\,j_{\max}}^{\rightarrow}$ to $j_{\max}$, and Dirac binding energy $E_{n,\,j_{\max}}^{\mathrm{Dirac}}$ based on DR resonance group energies $\bar{E}_{\mathrm{DR}}$ for different states (see text). Averaging yields the final excitation energies $E_{\mathrm{ex}}(2s \to 2p_{\bar{j}})$. All energies are given in eV.

State	$j_{\max}$	$\bar{E}_{\mathrm{DR}}$	$E_{\mathrm{DR},\,j_{\max}}^{\rightarrow}$	$E_{n,\,j_{\max}}^{\mathrm{Dirac}}$	E_{ex}
		$2s \to 2p_{1/2}$			
$18_{1/2}$	35/2	9.490(29)	1.088(30)	109.235	119.813 (42)
$18_{>1/2}$	35/2	10.447(30)	0.138(30)	109.235	119.820 (42)
			$E_{\mathrm{ex}}(2s \to 2p_{1/2})$		119.816(42)
		$2s \to 2p_{3/2}$			
$9s_{1/2}$	17/2	45.815(43)	9.123(30)	437.081	492.019 (52)
$9p_{1/2}$	17/2	47.307(43)	7.801(30)	437.081	492.189 (52)
$9p_{3/2}$	17/2	50.939(44)	4.107(30)	437.081	492.127 (52)
$9d_{3/2}$	17/2	52.075(44)	3.036(30)	437.081	492.192 (52)
$9l_{>3/2}$	17/2	54.316(44)	0.789(30)	437.081	492.186 (53)
			$E_{\mathrm{ex}}(2s \to 2p_{3/2})$		492.142(52)
		Without $9s_{1/2}$ (see text):	$E_{\mathrm{ex}}(2s \to 2p_{3/2})$		492.174(52)

Final excitation energies $E_{\mathrm{ex}}(2s \to 2p_{1/2})$ and $E_{\mathrm{ex}}(2s \to 2p_{3/2})$ are derived as weighted averages of the individual data for E_{ex} in Table I. Since our errors are mainly systematic, the final uncertainty is not reduced due to the averaging. For the $2s \to 2p_{3/2}$ excitation the energy as derived from $(2p_{3/2}9s_{1/2})_J$ resonances at 46 eV is significantly lower than for the other four groups. A corresponding mismatch between the MCDF calculations for the $n = 9$ fine-structure splitting of the $p_{3/2}$ resonances and our experimental data was already discussed in Sec. IV B (compare to Fig. 5). In order to account for this wrong bias on the excitation energy we treat the $(2p_{3/2}9s_{1/2})_J$ resonance group as an outlier and exclude it from the final determination of the $E_{\mathrm{ex}}(2s \to 2p_{3/2})$ excitation energy. For comparison, in Table I we also provide the $2p_{3/2}$ excitation energy based on all five resolved groups.

1. Discussion

In Table II and Fig. 9 we compare the results for the $2s$-$2p_{1/2}$ and $2s$-$2p_{3/2}$ transition energies from this work with a compilation of data from earlier experimental [6,9–11] and theoretical [13,14,45–50] works. For both transitions an excellent agreement of our values and the other measured excitation energies is found. The same holds true for the comparison of our work with theory if one excludes the $E(2s$-$2p_{1/2})$ calculation of Indelicato and Desclaux from 1990. Interestingly, though, their $2p_{3/2}$ value is in good agreement with the other calculations and all experimental data.

For the $2p_{1/2}$ excitation our collision spectroscopy result is by far not as precise as the x-ray spectroscopy data of Feili *et al.* [9] and of Träbert *et al.* [6]. In contrast, for the $2s$-$2p_{3/2}$ transition we were able to reduce the uncertainties

TABLE II. Experimental and theoretical values for the $2s$-$2p_{1/2}$ and $2s$-$2p_{3/2}$ transition energies for ${}^{A}\mathrm{Xe}^{51+}$. All energies are given in eV. Please note that different isotopes (A) were used in the studies. Abbreviations used in the table are as follows: DR (dielectronic recombination), beam-foil (beam-foil spectroscopy), S-EBIT (super electron-beam ion-trap spectroscopy), QED (QED perturbation theory), R/MBPT (relativistic or many-body perturbation theory), RCI (relativistic configuration interaction), and MCDF (multiconfiguration Dirac-Fock).

	Year	Method	A	$2s \rightarrow 2p_{1/2}$	$2s \rightarrow 2p_{3/2}$
		Experiment			
This work	2014	DR	136	119.816(42)	492.174(52)
Träbert *et al.* [6]	2003	S-EBIT	mix	119.811(12)	
Feili *et al.* [9]	2000	Beam-foil	124	119.820(8)	
Büttner *et al.* [11]	1992	Beam-foil	136	119.91(23)	492.20(98)
Martin *et al.* [10]	1989	Beam-foil	–	119.965(93)	492.39(59)
		Theory			
Sapirstein & Cheng [45]	2011	S-matrix	–	119.821	492.206
Kozhedub *et al.* [14]	2010	QED	132	119.831(6)	492.225(6)
Yerokhin *et al.* [13]	2007	QED	132	119.820(40)	
Chen *et al.* [46]	1995	RCI	–	119.82	492.21
Blundell [47]	1993	RMBPT	–	119.84(1)	492.22
Kim *et al.* [48]	1991	RMBPT & MCDF	–	119.82	492.18
Indelicato & Desclaux [49]	1990	MCDF	–	119.9	492.21
Seely [50]	1989	MBPT & MCDF	–	119.822	492.22

by more than an order of magnitude compared to previous measurements. We would like to emphasize that our approach by means of electron-ion collision spectroscopy fundamentally differs from the other measurements that are based on the precise determination of the wavelength of emitted photons. Hence, the present work is an important benchmark of the collision spectroscopy technique, in particular, since for U^{89+} a slight disagreement between DR spectroscopy [4] and x-ray spectroscopy is noted [7].

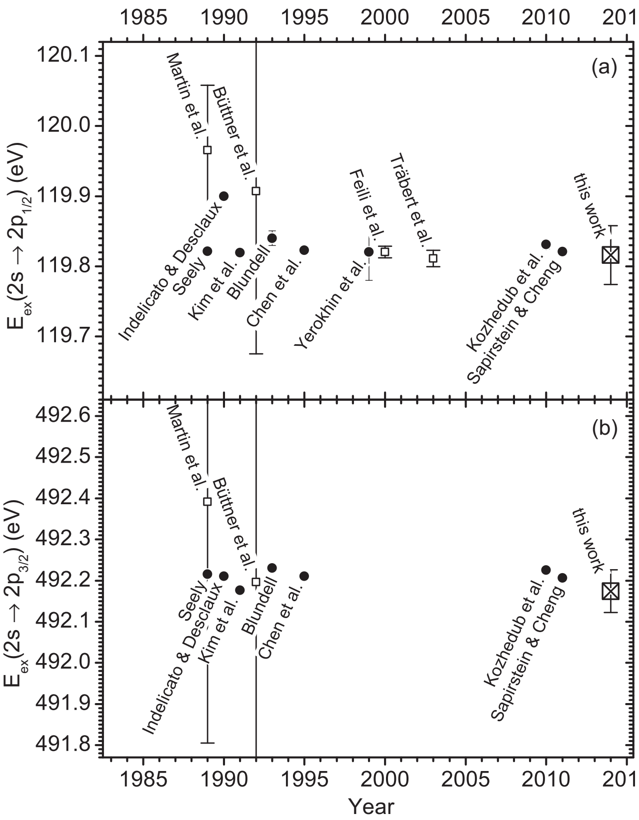

FIG. 9. $\Delta n = 0$ transition energies in ${}^{A}\mathrm{Xe}^{51+}$. This work (☒), previous experimental results (☐) [6,9–11], and theory (●) [13,14,45–50]. Panel (a) shows data for the $2s$-$2p_{1/2}$ transition, and panel (b) that for the $2s$-$2p_{3/2}$ transition. The data are the same as in Table II.

The individual experiments and calculations use different isotopes or nuclear charge radii in their determination of the excitation energy (see Table II). Xenon possesses natural isotopes from $A = 124$ to $A = 136$. Applying the results of Li *et al.* [51] and nuclear mean-square radii from Angeli [52], the volume shift amounts to ~4 meV for both transitions, and the mass shifts are even smaller. On the present level of experimental accuracy the differences of the isotopes used in the studies is not important. We do not consider magnetic hyperfine splitting (HFS) here; however, in the work of Martin *et al.* [10] and Träbert *et al.* [6], odd isotopes of xenon might have been present. Our experimental results are sensitive to one-loop QED contributions on a level <1% and to the screened QED contributions on a level ~15%. The experiment, however, is not yet precise enough to test the relativistic recoil part and two-loop QED contributions (compare Table III).

TABLE III. QED contributions to the $2s$-$2p_{1/2}$ and to the $2s$-$2p_{3/2}$ transition energies in Li-like xenon ions ${}^{132}\mathrm{Xe}^{51+}$ according to Kozhedub *et al.* [14]. All values are given in eV.

Contribution	$2s$-$2p_{1/2}$	$2s$-$2p_{3/2}$
Electronic structure	126.1471(31)	497.8958(31)
One-loop QED	−6.6851	−5.9880
Screened QED	0.3773(32)	0.3303(31)
Recoil	−0.0257	−0.0278
Two-loop QED	0.0175(40)	0.0152(40)
Total theory	119.831(6)	492.225(6)

TABLE IV. Scaled experimental $S' = Sp^2n^3$ and theoretical $S'_T = S_T p_T^2 n^3$ resonance strengths (in cm^2 eV^3 c^{-2}) and mean resonance energies $\bar{E}_{\mathrm{DR}}$ (in eV) for the DR process $2s + e^- \to 2p_{1/2}nl_j$.

nl_j	$\bar{E}_{\mathrm{DR}}$	S'	S'_T
$18l_{1/2}$	9.490	0.011 ± 0.002	0.008
$18l_{j>1/2}$	10.447	0.132 ± 0.022	0.116
$19l_{1/2}$	20.849	0.009 ± 0.002	0.012
$19l_{j>1/2}$	21.658	0.125 ± 0.021	0.123
$20l_j$	31.181	0.130 ± 0.022	0.098
$21l_j$	39.426	0.133 ± 0.023	0.143
$22l_j$	46.569	0.144 ± 0.025	0.145
$23l_j$	*Blended with* $2p_{3/2}$ $9l_j$		0.146
$24l_j$	58.269	0.127 ± 0.022	0.147
$25l_j$	63.103	0.125 ± 0.021	0.149
$26l_j$	67.380	0.126 ± 0.021	0.150
$27l_j$	71.188	0.125 ± 0.021	0.151
$28l_j$	74.602	0.128 ± 0.022	0.152
$29l_j$	77.684	0.121 ± 0.021	
$30l_j$	80.464	0.124 ± 0.021	
$31l_j$	82.930	0.129 ± 0.022	
$32l_j$	85.191	0.124 ± 0.023	
$33l_j$	87.310	0.120 ± 0.021	
$34l_j$	89.180	0.117 ± 0.021	
$35l_j$	90.873	0.122 ± 0.021	
$36l_j$	92.461	0.103 ± 0.019	
$37l_j$	93.963	0.117 ± 0.030	
$38l_j$	95.279	0.120 ± 0.022	
$39l_j$	96.515	0.123 ± 0.023	
$40l_j$	97.674	0.122 ± 0.023	
$41l_j$	98.713	0.106 ± 0.020	
$42l_j$	99.727	0.106 ± 0.031	
$43l_j$	100.632	0.104 ± 0.025	

E. Resonance strengths

Weighted mean resonance energies $\bar{E}_{\mathrm{DR}}$ (compare Sec. IV D) and absolute DR resonance strengths were extracted from the present measurement by integration of the peak areas taking into account the experimental response function (see Sec. III C). The derived resonance strengths S_E of well-separated resonances are listed in Tables IV and V for the $(2p_{1/2}nl_j)$ and $(2p_{3/2}nl_j)$ resonance series, respectively. For comparison, the corresponding calculated MCDF resonance strengths S_T (see Sec. II) are provided. Rydberg resonances are experimentally resolved up to $n = 43$ and $n = 36$ for the series $2p_{1/2}nl_j$ and $2p_{3/2}nl_j$, respectively. Some resonance groups are blended by other DR resonances. If both resonances show significant resonance strengths, the measured resonance strengths can not be attributed clearly to one of the resonances. The presented (measured and calculated) resonance strengths were scaled by the dominant expected proportionalities, that is, $S \propto p^{-2}n^{-3}$, compare Eq. (3) and [21]. For the overlapping unresolved resonances $n \geqslant 44$ $(2p_{1/2}nl_j)$ and $n \geqslant 37$ $(2p_{3/2}nl_j)$, the resonance strengths are estimated from the resonance continuum $n \to \infty$. Only quantum numbers up to $n_{\mathrm{fi}} \sim 110$ that survive field ionization in the ring dipole magnet are considered.

TABLE V. Same as Table IV but for the $2s + e^- \to 2p_{3/2}nl_j$ resonance series.

nl_j	$\bar{E}_{\mathrm{DR}}$	S'	S'_T
$9s_{1/2}$	45.831	0.006 ± 0.001	0.005
$9p_{1/2}$	47.307	0.007 ± 0.001	0.005
$9p_{3/2}$	50.939	0.006 ± 0.001	0.005
$9d_{3/2}$	52.075	0.019 ± 0.003	0.014
$9l_{j>3/2}$	54.316	0.189 ± 0.032	0.161
$10l_{1/2}$	131.923	0.012 ± 0.002	0.012
$10l_{j>1/2}$	137.384	0.195 ± 0.033	0.219
$11l_{1/2}$	194.880	0.012 ± 0.002	0.013
$11l_{j>1/2}$	199.010	0.194 ± 0.033	0.229
$12l_{1/2}$	242.653	0.011 ± 0.002	0.013
$12l_j$	245.865	0.198 ± 0.034	0.239
$13l_j$	282.161	0.218 ± 0.037	0.261
$14l_j$	311.099	0.217 ± 0.037	0.271
$15l_j$	334.442	0.235 ± 0.040	0.281
$16l_j$	353.536	0.250 ± 0.043	0.290
$17l_j$	369.371	0.255 ± 0.043	0.301
$18l_j$	382.635	0.269 ± 0.046	0.311
$19l_j$	393.831	0.283 ± 0.048	0.321
$20l_j$	403.432	0.294 ± 0.050	0.330
$21l_j$	411.668	0.298 ± 0.051	0.344
$22l_j$	418.804	0.309 ± 0.052	0.356
$23l_j$	425.008	0.308 ± 0.052	0.366
$24l_j$	430.502	0.311 ± 0.053	0.377
$25l_j$	435.332	0.330 ± 0.056	0.385
$26l_j$	439.618	0.349 ± 0.059	0.400
$27l_j$	443.440	0.362 ± 0.062	0.404
$28l_j$	446.861	0.357 ± 0.061	0.412
$29l_j$	449.912	0.375 ± 0.064	
$30l_j$	452.693	0.395 ± 0.067	
$31l_j$	455.228	0.422 ± 0.072	
$32l_j$	457.500	0.417 ± 0.071	
$33l_j$	459.547	0.439 ± 0.075	
$34l_j$	461.479	0.434 ± 0.074	
$35l_j$	463.243	0.511 ± 0.087	
$36l_j$	464.825	0.507 ± 0.086	

Figure 10 summarizes our experimental and theoretical results for the DR resonance strengths. The uncertainty $\Delta S'$ of the experimental resonance strengths given in Tables IV and V is predominantly caused by the systematic 17% uncertainty of the measured DR-rate coefficient (see Sec. IV A).

Experiment and MCDF calculations for the resonance strengths agree well within the error bars, albeit just. For the majority of the resonances the theoretical resonance strength is by about 15% larger than the experimental one. Exceptions are the $n = 18,19,20$ resonance groups of the $2p_{1/2}$ resonance series and the $n = 9$ resonance group of the $2p_{3/2}$ resonance series. In these cases, the theoretical values are slightly lower or match the experimental ones. In all cases the shape, that is, the distribution of the resonance strengths within one n manifold, is well reproduced. For details, compare Secs. IV A and IV B, in particular Figs. 6 and 5. Experimental and theoretical data sets show the same n dependency of resonance strengths (Fig. 10). Similarly to the $(2p_{1/2}nl_j)$ resonances in Li-like Pb^{79+} [21,42] the measured resonance strength for the $2p_{1/2}$ series follow an n^{-3} scaling (Fig. 10). The n^{-3} dependency of Rydberg DR resonances is a common notion in the literature

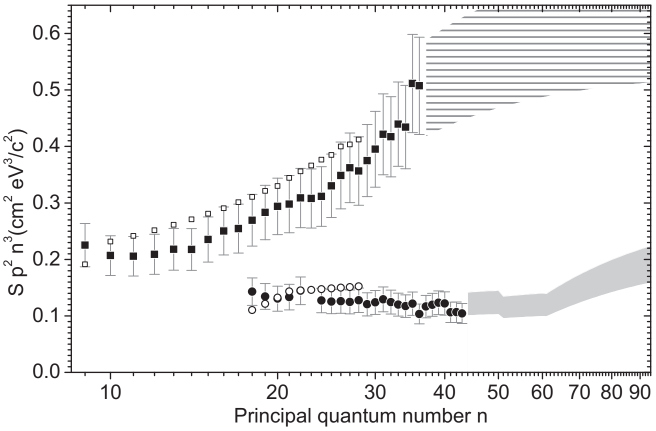

FIG. 10. Measured and theoretical scaled DR resonance strengths for $\Delta n = 0$ DR in $^{136}\mathrm{Xe}^{51+}$. Experimental data for $2s + e^- \rightarrow 2p_{1/2}n$ (●) and $2s + e^- \rightarrow 2p_{3/2}n$ (■). Open symbols (○ and □) show the corresponding results of the present MCDF calculations. Shaded and hatched areas show the resonance strengths as derived from the experiment for unresolved very high principal quantum numbers n.

[53–56] that, however, has to be treated with some caution: The basis of the n^{-3} rule is again that the mutual overlap of the wave functions of the core electron and the Rydberg electron decreases for increasing principle quantum number n. In this case, Auger rates predominantly scale as propto n^{-3}, and the radiative decay takes place via a fast dipole transition of the Rydberg electron to one of the lower-n states (type II) in which radiative rates are $\propto n^{-3}\nu^{-1}$, with $h\nu$ being the energy of the emitted photon. At the same time, the transition rate of the core electron (type I) stays constant.

With $\Gamma_{\mathrm{I}}^{\mathrm{rad}} = \sum_{\mathrm{typeI}} \Gamma_{d\to f''}^{\mathrm{rad}}$ and $\Gamma_{\mathrm{II}}^{\mathrm{rad}} = \sum_{\mathrm{typeII}} \Gamma_{d\to f''}^{\mathrm{rad}}$ for the radiative width of core and Rydberg electron, respectively, and $\Gamma^{\mathrm{rad}} = \Gamma_{\mathrm{I}}^{\mathrm{rad}} + \Gamma_{\mathrm{II}}^{\mathrm{rad}}$ for the total radiative width of the intermediate state from Eq. (3) we obtain for our simplified model with one autoionization channel only:

$$\sigma_{\mathrm{tot}}^{\mathrm{DR}} \propto \frac{1}{E_{\mathrm{el}}} \Gamma^{\mathrm{Aug}} \frac{\Gamma_{\mathrm{I}}^{\mathrm{rad}} + \Gamma_{\mathrm{II}}^{\mathrm{rad}}}{\Gamma^{\mathrm{Aug}} + \Gamma_{\mathrm{I}}^{\mathrm{rad}} + \Gamma_{\mathrm{II}}^{\mathrm{rad}}}, \tag{17}$$

that is, the product of autotionization width and fluorescence yield $\omega_{d\to f}$. Hence from this formula it is easy to see that the *slower* of the two rates, Auger or radiative, determines the cross section while the *faster* yields the natural width of the resonance.

For two limiting cases one immediately arrives at an n^{-3} scaling (cf. in Refs. [56–58]) for the total cross section [55]: For $\Gamma^{\mathrm{Aug}} \ll \Gamma^{\mathrm{rad}}$ the fluorescence yield $\omega_{d\to f} \simeq 1$ and $\sigma^{\mathrm{DR}} \propto \Gamma^{\mathrm{Aug}}$. This is the case for heavy highly charged ions as the Xe^{51+} under investigation. Alternatively, for $\Gamma^{\mathrm{Aug}} \gg \Gamma^{\mathrm{rad}}$ and $\Gamma_{\mathrm{I}}^{\mathrm{rad}} \ll \Gamma_{\mathrm{II}}^{\mathrm{rad}}$ the cross section $\sigma^{\mathrm{DR}} \propto \Gamma_{\mathrm{II}}^{\mathrm{rad}}$ and thus again $\sigma^{\mathrm{DR}} \propto n^{-3}$.

In both cases one has to take into account that for increasing n at some point the constant $\Gamma_{\mathrm{I}}^{\mathrm{rad}}$ of the core electron will become the dominant decay channel and will lead to a deviation from n^{-3}. For the present case of the $p_{1/2}$ resonances of Xe^{51+} this takes place roughly at $n = 60 \ldots 80$ and is visible in Fig. 10 for the unresolved resonance strengths towards the series limits.

The toy model above will fail if core excitations proceed into higher excited atomic states. This is the case already for the $2s \rightarrow 2p_{3/2}$ series of our Xe^{51+}. The doubly-excited $2p_{3/2}nl_j$ configurations allow more options for the decay channels, for instance, a second strong Auger channel or cascades of radiative and Auger transitions to below the auotionization threshold. In fact, for the $\mathrm{Xe}^{50+}(2p_{3/2}nl_j)$ resonances we notice for the resonance strength a behavior $\propto n^{-2.3}$.

For further details about high-n Rydberg states and their properties and scalings we refer to Refs. [36,53–56,59,60].

V. SUMMARY AND OUTLOOK

We have measured the recombination rate coefficient for dielectronic recombination of Xe^{51+} forming Xe^{50+}. An electron-ion merged-beams configuration was used at the heavy-ion storage ring ESR. The measurement covers a collision energy range from 0 to 505 eV and includes all $\Delta n = 0$ DR resonances in Li-like xenon, that is, all DR processes $2s + e^- \rightarrow 2p_{1/2}nl_j$ and $2s + e^- \rightarrow 2p_{3/2}nl_j$ up to the respective series limits $n \rightarrow \infty$.

Individual resonances were resolved and their resonance strengths were extracted for Rydberg-resonance manifolds with principal quantum numbers n up to 43 for the $2p_{1/2}$ excitation and up to $n = 36$ for the $2p_{3/2}$ series. Our measurement is compared with results from MCDF theory. A good agreement of the experiment and our MCDF calculation for the recombination spectra and the absolute resonance strengths is found. In particular, the calculations are in excellent agreement within a Rydberg manifold with given n. For the $2p_{1/2}$ series we find a trend of the resonance strength $\propto n^{-3}$ and for the $2p_{3/2}$ series a dependency close to $n^{-2.3}$.

The excitation energies $E(2s \rightarrow 2p_{1/2})$ and $E(2s \rightarrow 2p_{3/2})$ were precisely determined by means of DR collision spectroscopy with values of $E(2s \rightarrow 2p_{1/2}) = 119.816(42)$ eV and $E(2s \rightarrow 2p_{3/2}) = 492.174(52)$ eV. Our error bars for both excitations are about the same and are mainly limited due to the imperfect knowledge about the transversal electron beam temperatures and according energy shifts. The $2s$-$2p_{1/2}$ transition energy is not as precise as the ones from x-ray techniques, but the comparison of the different methods provides an important benchmark of the DR approach and setup. From the same measurement the energy for the $2p_{3/2}$ excitation is derived and its uncertainty compared to previous studies is improved by more than an order of magnitude.

Within the extension of the present heavy-ion facilities at the GSI-Helmholtzentrum für Schwerionenforschung towards the international Facility for Anti-proton and Ion Research (FAIR) [61] at the same site the former CRYRING storage ring of the Manne-Siegbahn laboratory in Stockholm is presently being relocated to Darmstadt and will be reinstalled at FAIR within the next 2 years [62]. At GSI/FAIR the former CRYRING will serve as a low-energy storage ring (LSR). The CRYRING/LSR is equipped with an electron cooler with electrons that are exceptionally cold in transversal direction due to adiabatic magnetic expansion of the electron beam [63].

Experiments in Stockholm at the CRYRING [15,23,63] have demonstrated transversal and longitudinal electron temperatures of $k_B T_\perp = 1.5$ meV and $k_B T_\parallel = 50$ μeV, respectively, to be compared to the present ESR experiment with $k_BT_\perp = 120$ meV and $k_BT_\parallel = 200$ μeV. The decrease of $T_\parallel$ and $T_\perp$ by factors of 80 and 4 will lead to significant reductions of the experimental energy spread and resolution, refer to Eq. (10) and Ref. [16]. In addition, the uncertainty due to the transversal temperature becomes smaller by nearly two orders of magnitude and, thus, the according uncertainties will be significantly reduced down to the 1-meV range. The potential of cold electron targets has already been exploited for many-electron cases at the CRYRING in Stockholm [15] and for few-electron medium-Z ions [3] at the TSR storage ring of the Max-Planck Institute for Nuclear Physics in Heidelberg. At GSI/FAIR the combination of a very capable injector that can deliver highly charged ions up to bare uranium or even intense beams of radioisotopes will boost precision, sensitivity, and extend the scope of topics. For very heavy ions uncertainties of the order of 1 meV will provide conclusive tests of higher-order contributions of QED in strong fields as well as to physics at the interface of electrons and atomic nucleus such as nuclear size, nuclear shape, hyperfine, and even nuclear polarization effects [16].

ACKNOWLEDGMENTS

We thank the GSI accelerator and ESR groups for their excellent support. Financial support by the German Federal Ministry for Education and Research (BMBF) (Contracts No. 06GI947 and No. 06GI7127/05P12R6FAN) and Deutsche Forschungsgemeinschaft (DFG) (Contract No. Schi378/8-1) is gratefully acknowledged. The work of D.B., C.B. and Z.H. was supported by the Alliance Program of the Helmholtz Association (HA216/EMMI).

[1] W. R. Johnson and G. Soff, At. Data Nucl. Data Tables **33**, 405 (1985).

[2] P. J. Mohr, G. Plunien, and G. Soff, Phys. Rep. **293**, 227 (1998).

[3] M. Lestinsky, E. Lindroth, D. A. Orlov, E. W. Schmidt, S. Schippers, S. Böhm, C. Brandau, F. Sprenger, A. S. Terekhov, A. Müller, and A. Wolf, Phys. Rev. Lett. **100**, 033001 (2008).

[4] C. Brandau, C. Kozhuharov, A. Müller, W. Shi, S. Schippers, T. Bartsch, S. Böhm, C. Böhme, A. Hoffknecht, H. Knopp, N. Grün, W. Scheid, T. Steih, F. Bosch, B. Franzke, P. H. Mokler, F. Nolden, M. Steck, T. Stöhlker, and Z. Stachura, Phys. Rev. Lett. **91**, 073202 (2003).

[5] J. Schweppe, A. Belkacem, L. Blumenfeld, N. Claytor, B. Feinberg, H. Gould, V. E. Kostroun, L. Levy, S. Misawa, J. R. Mowat, and M. H. Prior, Phys. Rev. Lett. **66**, 1434 (1991).

[6] E. Träbert, P. Beiersdorfer, J. K. Lepson, and H. Chen, Phys. Rev. A **68**, 042501 (2003).

[7] P. Beiersdorfer, H. Chen, D. B. Thorn, and E. Träbert, Phys. Rev. Lett. **95**, 233003 (2005).

[8] S. W. Epp, J. R. Crespo López-Urrutia, G. Brenner, V. Mäckel, P. H. Mokler, R. Treusch, M. Kuhlmann, M. V. Yurkov, J. Feldhaus, J. R. Schneider, M. Wellhöfer, M. Martins, W. Wurth, and J. Ullrich, Phys. Rev. Lett. **98**, 183001 (2007).

[9] D. Feili, P. Bosselmann, K.-H. Schartner, F. Folkmann, A. E. Livingston, E. Träbert, X. Ma, and P. H. Mokler, Phys. Rev. A **62**, 022501 (2000).

[10] S. Martin, J. P. Buchet, M. C. Buchet-Poulizac, A. Denis, J. Desesquelles, M. Druetta, J. P. Grandin, D. Hennecart, X. Husson, and D. Lecler, Europhys. Lett. **10**, 645 (1989).

[11] R. Büttner, B. Kraus, K. H. Schartner, F. Folkmann, P. H. Mokler, and G. Müller, Z. Phys. D: Atoms, Molec. Cluster. **22**, 693 (1992).

[12] V. A. Yerokhin, P. Indelicato, and V. M. Shabaev, Phys. Rev. Lett. **97**, 253004 (2006).

[13] V. A. Yerokhin, A. N. Artemyev, and V. M. Shabaev, Phys. Rev. A **75**, 062501 (2007).

[14] Y. S. Kozhedub, A. V. Volotka, A. N. Artemyev, D. A. Glazov, G. Plunien, V. M. Shabaev, I. I. Tupitsyn, and T. Stöhlker, Phys. Rev. A **81**, 042513 (2010).

[15] E. Lindroth, H. Danared, P. Glans, Z. Pesic, M. Tokman, G. Vikor, and R. Schuch, Phys. Rev. Lett. **86**, 5027 (2001).

[16] C. Brandau and C. Kozhuharov, in *Atomic Processes in Basic and Applied Physics*, Springer Series on Atomic, Optical, and Plasma Physics, edited by V. Shevelko and H. Tawara (Springer, Berlin, 2012), Vol. 68, p. 283.

[17] C. Brandau, C. Kozhuharov, Z. Harman, A. Müller, S. Schippers, Y. S. Kozhedub, D. Bernhardt, S. Böhm, J. Jacobi, E. W. Schmidt, P. H. Mokler, F. Bosch, H.-J. Kluge, T. Stöhlker, K. Beckert, P. Beller, F. Nolden, M. Steck, A. Gumberidze, R. Reuschl, U. Spillmann, F. J. Currell, I. I. Tupitsyn, V. M. Shabaev, U. D. Jentschura, C. H. Keitel, A. Wolf, and Z. Stachura, Phys. Rev. Lett. **100**, 073201 (2008).

[18] S. Schippers, E. W. Schmidt, D. Bernhardt, D. Yu, A. Müller, M. Lestinsky, D. A. Orlov, M. Grieser, R. Repnow, and A. Wolf, Phys. Rev. Lett. **98**, 033001 (2007).

[19] S. Schippers, D. Bernhardt, A. Müller, M. Lestinsky, M. Hahn, O. Novotný, D. W. Savin, M. Grieser, C. Krantz, R. Repnow, and A. Wolf, Phys. Rev. A **85**, 012513 (2012).

[20] D. Bernhardt, C. Brandau, Z. Harman, C. Kozhuharov, A. Müller, W. Scheid, S. Schippers, E. W. Schmidt, D. Yu, A. N. Artemyev, I. I. Tupitsyn, S. Böhm, F. Bosch, F. J. Currell, B. Franzke, A. Gumberidze, J. Jacobi, P. H. Mokler, F. Nolden, U. Spillman, Z. Stachura, M. Steck, and T. Stöhlker, Phys. Rev. A **83**, 020701 (2011).

[21] C. Brandau, T. Bartsch, A. Hoffknecht, H. Knopp, S. Schippers, W. Shi, A. Müller, N. Grün, W. Scheid, T. Steih, F. Bosch, B. Franzke, C. Kozhuharov, P. H. Mokler, F. Nolden, M. Steck, T. Stöhlker, and Z. Stachura, Phys. Rev. Lett. **89**, 053201 (2002).

[22] A. Müller and S. Schippers, in *Atomic Processes in Basic and Applied Physics*, Springer Series on Atomic, Optical, and Plasma Physics, edited by V. Shevelko and H. Tawara (Springer, Berlin, 2012), Vol. 68, pp. 25–35.

[23] R. Schuch and S. Böhm, J. Phys. Conf. Ser. **88**, 012002 (2007).

[24] A. Müller, Adv. At. Mol. Phys. **55**, 293 (2008).

[25] S. L. Haan and V. L. Jacobs, Phys. Rev. A **40**, 80 (1989).

[26] P. Zimmerer, N. Grün, and W. Scheid, Phys. Lett. A **148**, 457 (1990).

[27] K. G. Dyall, I. P. Grant, C. T. Johnson, F. A. Parpia, and E. P. Plummer, Comput. Phys. Commun. **55**, 425 (1989).

[28] F. A. Parpia, C. F. Fischer, and I. P. Grant, Comput. Phys. Commun. **94**, 249 (1996).

[29] B. Franzke, Nucl. Instrum. Methods B **24-25**, 18 (1987).

[30] H. Poth, Phys. Rep. **196**, 135 (1990).

[31] M. Steck, P. Beller, K. Beckert, B. Franzke, and F. Nolden, Nucl. Instrum. Methods A **532**, 357 (2004).

[32] H. Horneff, Patent DE 4040164 C2, German Patent and Trademark Office, 1992.

[33] S. Schippers, T. Bartsch, C. Brandau, A. Müller, G. Gwinner, G. Wissler, M. Beutelspacher, M. Grieser, A. Wolf, and R. A. Phaneuf, Phys. Rev. A **62**, 022708 (2000).

[34] H. Poth, B. Seligmann, W. Schwab, M. Wörtge, A. Wolf, R. Conti, W. Frieze, D. Gidley, A. Rich, M. Skalsey, J. V. House, P. Zitzewitz, J. Berger, P. Blatt, R. Neumann, and G. zu Putlitz, Hyperfine Interact. **44**, 257 (1988).

[35] A. Müller, Phil. Trans. R. Soc. London Ser. A **357**, 1279 (1999).

[36] C. Brandau, Ph.D. thesis, Justus-Liebig-Universität, Gießen, 2000.

[37] M. Reiser, *Theory and Design of Charged Particle Beams* (John Wiley & Sons, New York, 1994).

[38] H. A. Bethe and E. E. Salpeter, *Quantum Mechanics of One-and Two-Electron Atoms* (Springer, Berlin, 1957).

[39] L. H. Andersen and J. Bolko, Phys. Rev. A **42**, 1184 (1990).

[40] A. Müller and S. Schippers, in *The Physics of Multiply and Highly Charged Ions*, edited by F. Currell (Kluwer Academic, Dordrecht, 2003), Vol. 1, pp. 269–301.

[41] M. Stobbe, Ann. Phys. (Leipzig) **7**, 661 (1930).

[42] N. R. Badnell, D. M. Mitnik, M. S. Pindzola, S. D. Loch, and S. A. Abdel-Naby, Phys. Rev. A **70**, 054701 (2004).

[43] W. Spies, O. Uwira, A. Müller, J. Linkemann, L. Empacher, A. Frank, C. Kozhuharov, P. H. Mokler, F. Bosch, O. Klepper, B. Franzke, and M. Steck, Nucl. Instrum. Methods B **98**, 158 (1995).

[44] D. Bernhardt, C. Brandau, Z. Harman, C. Kozhuharov, S. Böhm, F. Bosch, S. Fritzsche, J. Jacobi, S. Kieslich, K. H., P. H. Mokler, F. Nolden, W. Shi, Z. Stachura, M. Steck, T. Stöhlker, A. Müller, and S. Schippers, J. Phys. B (to be published).

[45] J. Sapirstein and K. T. Cheng, Phys. Rev. A **83**, 012504 (2011).

[46] M. H. Chen, K. T. Cheng, W. R. Johnson, and J. Sapirstein, Phys. Rev. A **52**, 266 (1995).

[47] S. A. Blundell, Phys. Rev. A **47**, 1790 (1993).

[48] Y.-K. Kim, D. H. Baik, P. Indelicato, and J. P. Desclaux, Phys. Rev. A **44**, 148 (1991).

[49] P. Indelicato and J. P. Desclaux, Phys. Rev. A **42**, 5139 (1990).

[50] J. F. Seely, Phys. Rev. A **39**, 3682 (1989).

[51] J. Li, C. Nazé, M. Godefroid, S. Fritzsche, G. Gaigalas, P. Indelicato, and P. Jönsson, Phys. Rev. A **86**, 022518 (2012).

[52] I. Angeli, At. Data Nucl. Data Tables **87**, 185 (2004).

[53] M. Scheer, R. C. Bilodeau, J. Thogersen, and H. K. Haugen, Phys. Rev. A **57**, 1493 (1998).

[54] Y. Hahn and K. J. LaGattuta, Phys. Rep. **166**, 195 (1988).

[55] J.-G. Wang, T. Kato, and I. Murakami, Phys. Rev. A **60**, 2104 (1999).

[56] Y. Hahn, Adv. At. Mol. Phys. **21**, 123 (1985).

[57] K.R. Karim and C.P. Bhalla, Phys. Rev. A **37**, 2599 (1988).

[58] C. J. Romanik, Astrophys. J. **330**, 1022 (1988).

[59] T. F. Gallagher, *Rydberg Atoms* (Cambridge University Press, Cambridge, 1994).

[60] M. J. Seaton, Rep. Prog. Phys. **46**, 167 (1983).

[61] http://www.fair-center.eu, retrieved 11/15/2014.

[62] M. Lestinsky, N. Angert, R. Bär, R. Becker, M. Bevcic, U. Blell, W. Bock, A. Bräuning-Demian, H. Danared, O. Dolinsky, W. Enders, M. Engström, A. Fischer, B. Franzke, G. Gruber, P. Hülsmann, A. Källberg, O. Kester, C.-M. Kleffner, Y. A. Litvinov, C. Mühle, B. Müller, I. Pschorn, T. Radon, H. Ramakers, H. Reich-Sprenger, D. Reistad, G. Riefert, M. Schwickert, A. Simonsson, J. Sjöholm, O. Skeppstedt, M. Steck, T. Stöhlker, W. Vinzenz, and H. Welker, CRYRING@ESR: A study group report (unpublished) (2012), http://www.fair-center.eu/for-users/publications/experiment-collaboration-publications.html, as retrieved 01/18/2015.

[63] H. Danared, G. Andler, L. Bagge, C. J. Herrlander, J. Hilke, J. Jeansson, A. Källberg, A. Nilsson, A. Paál, K.-G. Rensfelt, U. Rosengård, J. Starker, and M. af Ugglas, Phys. Rev. Lett. **72**, 3775 (1994).